Hilbert fractal inspired dipoles for passive RF shimming in ultra-high field MRI

Tania Vergara Gomez, Marc Dubois, Kaizad Rustomji, Elodie Georget, Tryfon Antonakakis, Alexandre Vignaud, Stanislas Rapacchi, Olivier Girard, F. Kober, Stefan Enoch, et al.

Photonics and Nanostructures - Fundamentals and Applications 48 (2022) 100988

Contents lists available at ScienceDirect

Photonics and Nanostructures - Fundamentals and Applications

journal homepage: www.elsevier.com/locate/photonics

Hilbert fractal inspired dipoles for passive RF shimming in ultra-high field MRI

Tania S. Vergara Gomez [a,b], Marc Dubois [a,b], Kaizad Rustomji [c], Elodie Georget [c], Tryfon Antonakakis [c], Alexandre Vignaud [d], Stanislas Rapacchi [a], Olivier M. Girard [a], Frank Kober [a], Stefan Enoch [b], Redha Abdeddaim [b,*]

[a] Aix Marseille Univ, CNRS, CRMBM, Marseille, France
[b] Aix Marseille Univ, CNRS, Centrale Marseille, Institut Fresnel, Institut Marseille Imaging, Marseille, France
[c] Multiwave Imaging, Marseille, France
[d] CEA, DRF/Joliot/Neurospin, Université Paris-Saclay & CNRS, Gif-sur-Yvette Cedex, France

ARTICLE INFO

Keywords:
Passive RF shimming
Fractals
Hilbert curves
UHF MRI
Head imaging

ABSTRACT

Ultra-high field MRI head coils present a characteristic B_1^+ magnetic field distribution resulting in inhomogeneous signal and contrast over the image, affecting relevant regions of interest such as the temporal lobes of the brain and the cerebellum. This is a consequence of the spatially varying flip angle distribution attributed to the reduction of the electromagnetic wavelength inside the human tissues. Without radical changes in the experimental setup, this problem has been effectively targeted by different passive RF shimming approaches such as high permittivity dielectric pads or metamaterials. The latter, however, may potentially decrease the B_1^+ field in other relevant areas or compromise the patient's comfort. Here, we present a novel approach based on meander dipoles inspired from Hilbert fractals. The structures were designed and studied numerically using finite element simulations. Prototypes of the structures were printed and tested with a 1Tx/32Rx birdcage head coil on a 7 T MR scanner. We demonstrate a new device based on compact, thin and flexible design, able to improve the B_1^+ field over each temporal lobe without deterioration of the RF performances in other brain areas and with minimal impact on patient comfort.

1. Introduction

In ultra-high field (UHF) magnetic resonance imaging (MRI), a major criterion to assure quality images is the uniformity of the transmit magnetic field flux (B_1^+) generated by the radiofrequency (RF) coils. At 7 T MRI, the proton (^{1}H) Larmor frequency reaches 300 MHz. Due to the high relative permittivity of human tissues, the associated RF wavelength reduces to around 11 cm, which is comparable to the size of some of the human organs [1,2]. Consequently, spatially varying phase and amplitude of the RF fields generate B_1^+ inhomogeneities across the image. For head coils, these inhomogeneities lead to stronger excitation in the image center and poor excitation in the vicinity of the coil. Thus, signal losses become strongly visible in the temporal lobe regions of the image [3]. Different approaches have been implemented to improve B_1^+ field uniformity of transmit coils such as passive RF shimming [4–10] and active RF shimming [11–20].

Active RF shimming is based on RF coils with multiple independently controllable transmit elements or channels [21]. These additional degrees of freedom can be exploited for a suitable optimization strategy to mitigate B_1^+ inhomogeneities [22]. However, active RF shimming raises new challenges in terms of workflow and safety such as the control of power deposition [23]. In contrast, passive RF shimming is based on the insertion of passive structures between the subject and the coil. Devices such as high-permittivity dielectric pads [4–7] or metamaterials [8–10] have been explored. These structures are inductively coupled to the main transmit RF coil. Induced currents (displacement or conduction currents) generate a secondary RF field that redistributes the initial B_1^+ field.

Dielectric pads mainly composed of high-permittivity materials such as barium titanate ($BaTiO_3$) and calcium titanate ($CaTiO_3$) are based on the principle of displacement currents [5–7]. However, several studies have confirmed that targeting multiple regions of interest (ROI) in the

* Correspondence to: Institute Fresnel, Marseille, France.
E-mail address: redha.abdeddaim@fresnel.fr (R. Abdeddaim).

https://doi.org/10.1016/j.photonics.2021.100988
Received 18 August 2021; Received in revised form 22 December 2021; Accepted 22 December 2021
Available online 28 December 2021

brain remains challenging as the local B_1^+ field increase near the pad, it is often balanced by a reduction of B_1^+ elsewhere [7,24–26].

The metamaterial approach is based on the principle of hybridization modes using metallic wires or strips coupled to each other in a specific geometry [8,9], which can further be combined with dielectric pads [10]. In high field MRI, electric dipoles have demonstrated better transmit efficiency compared to simple loops [27–30]. This property has been used in metamaterials such as the Hybridized Meta-Atom (HMA) [8,9]. But, similarly to the dielectric pads, using several HMA structures to target multiple brain ROIs was shown to be difficult [31]. One way to tackle this issue would be reducing the dipole's length in order to minimize mutual interaction between the passive structures and facilitate their integration within commercial head coils.

Reduction of the dipole's length has been explored by adding reactive parts in the form of lumped elements [32] or meanders [16,33–35]. Our approach is to accomplish this reduction by designing a meander dipole based on a Hilbert fractal design. Fractals have indeed been widely exploited in the telecommunication domain for the reduction of antenna dimensions [36,37]. Hilbert fractal associated with RF surface coil was previously introduced in order to increase sensitivity away from the coil [38]. It was shown that the Hilbert fractal curves presented an electromagnetic response similar to a split-ring resonator. Here, we introduce a modified structure composed of two connected 3rd-order Hilbert curves in order to produce an electric dipole like response.

The main objective of this study was to develop passive RF shimming elements associated with a volume coil (birdcage) in order to enhance the B_1^+ field in each temporal lobe without deteriorating the B_1^+ field in

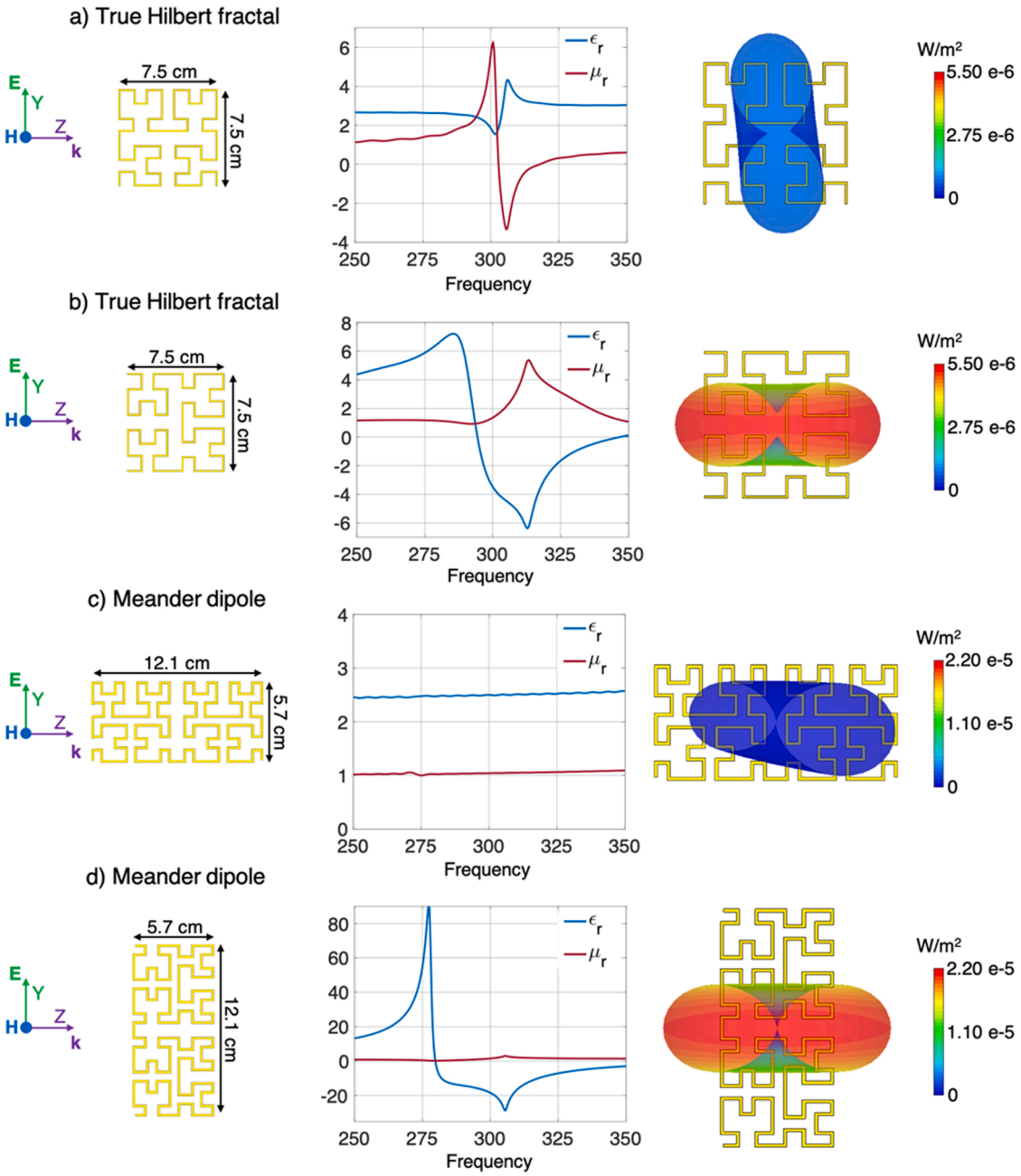

Fig. 1. Electromagnetic characteristics of the true Hilbert fractal and the meander dipole in two orientations. On the left, schematic of the passive structures placed on the YZ plane and the propagation of the incident EM wave. At the center a plot with the real part of the relative permittivity (ε_r) and the real part of the relative permeability (μ_r). On the right, the far field scattered power of each structure in W/m^2 with different color maps.

other relevant brain regions. We demonstrated numerically and experimentally that passive RF shimming in a 7 T MRI head coil was possible with electrically small dipole structures inspired by Hilbert fractals (e.g. length $\leq \lambda/10$). The introduced elements were compact, thin, flexible and free of lumped elements. Prototypes were built and characterized on an anthropomorphic phantom in conjunction with a commercial head coil at 7 T.

2. Material and methods

2.1. Numerical simulations of the meander dipoles

Numerical simulations were carried out using CST Microwave studio 2019 (Computer Simulation Technology GmbH, Darmstadt, Germany). The electromagnetic (EM) behavior of the meander dipole and the true Hilbert fractal was studied with two different setups: free space scatter diffraction under plane wave illumination and waveguide illumination. From the first setup, radar cross-section (RCS), defined as the ratio between the scattered power to the incident power of the plane wave, and far field diagrams were computed to show the nature of the structures' radiative EM mode. The studied structures were placed on the YZ plane and excited by a plane wave. The wavevector (k) of the incident plane wave propagated in z-axis while the electric (E) field was polarized along y-axis and the magnetic (H) field was polarized along x-axis (Fig. 1 on the left). In the second simulation setup, S-parameters coefficients were computed to retrieve electromagnetic properties such as the real part of the relative permittivity (ε_r) and the real part of the relative permeability (μ_r) [39–42]. The structures were placed on the YZ plane between two waveguide ports and excited by an EM wave propagating along the z-axis. The walls perpendicular to y-axis were defined as perfect H conductor boundaries and the walls perpendicular to the x-axis were defined as perfect E conductor boundaries. The walls were at 1 cm from all the edges of the structures to maintain the same periodicity condition. RCS of 2nd, 3rd and 4th fractal orders were calculated for the true Hilbert fractal and the meander dipole to optimize their lateral dimensions to reach a frequency of 305 MHz without the use of lumped elements. Based on our dimensions constrains, we chose to further analyze the 3rd-order Hilbert fractal (7.5 cm by 7.5 cm dimension, Fig. 1.a and b) and the meander dipole based on two 3rd-order Hilbert fractals connected in series (12.1 cm by 5.7 cm dimension, Fig. 1.c and d). The structures were simulated in metallic copper with a thickness of 0.05 cm and a width of 0.1 cm. The two structures were tested with two different orientations with respect to the incoming EM field.

In a second numerical study, the passive structures were inserted in a birdcage coil to study their shimming performances. We analyzed the generated magnetic (H) field components H_x and H_y and the resulting B_1^+ maps in a coronal slice with a homogeneous anthropomorphic phantom (relative permittivity $\varepsilon_r = 45.3$ and conductivity $\sigma = 0.87$ S/m). A 16-leg birdcage head coil was used with 25 cm inner diameter and 24 cm length, using a shield of 31 cm diameter. It had 2 power input ports placed 90° apart driven in quadrature to obtain circular polarization. On each port, L-shape matching circuits were added to tune and match the coil to the Larmor frequency (300 MHz) in presence of the phantom. The tested configurations were the birdcage coil alone as a reference, the two orientations of the true Hilbert fractal and the meander dipole. Single structures were placed on the right side of the phantom. The meander dipole and the Hilbert fractals were simulated as copper on a 0.4 mm-thick FR-4 substrate.

A second meander dipole was later added on the left side of the phantom with a central symmetry operation. Transmit B_1^+ field maps and profiles were obtained. The B_1^+ maps were normalized at 1 W stimulated power. We studied a central sagittal slice, a coronal slice and three different axial slices. The coronal slice was obtained at 2 cm from the center of the phantom towards the back of the head. The lower axial slice was obtained at 11 cm from the top of the head. The distance between the axial slices was 2.4 cm. Simulations with dielectric pads of relative permittivity $\varepsilon_r = 110$ were added for comparison. Dielectric pads with the same dimensions as the meander dipole were studied (12.1×5.7 cm^2) as well as previously reported dielectric pads dimensions (18×18 cm^2) [51]. Profiles were extracted only from the RF coil alone (ref) and the meander dipoles.

The meander dipoles were evaluated with the male body model Hugo from the voxel family using the same configuration (birdcage coil alone and birdcage coil with the meander dipoles) as that used with the homogeneous anthropomorphic phantom. B_1^+ maps and the respective profiles were calculated using 1 W stimulated power. The sagittal slice was taken in the center while the axial slice was taken at 8.4 cm from the top of the head and the coronal slice at 1.2 cm distance from the center. Global and local SAR were calculated.

2.2. Phantom experiments with two meander dipoles

The copper meander dipoles with dimensions of 12.1 cm by 5.7 cm (Fig. 3.a) were printed on a 0.4 mm-thick FR-4 substrate. For the validation, the experiments were performed in a 7 T MRI scanner (Magnetom, Siemens Healthineers, Erlangen, Germany). The reference images were obtained with a 1Tx/32Rx proton head coil (Nova Medical, Wilmington, MA, USA) using a specific anthropomorphic head phantom (SAM, SPEAG, Zurich, Switzerland) filled with a liquid of relative permittivity $\varepsilon_r = 45.3$ and conductivity $\sigma = 0.87$ S/m. The meander dipoles were placed on each side in direct contact with the phantom (Fig. 3.b-d) and with the same orientation as in the simulation (Fig. 2.d). Foam plastic spacers of 1 cm thickness were used as support onto the internal walls of the head coil.

B_1^+ field maps in coronal and axial orientation were acquired using a turbo-flash XFL MRI sequence [43]. The following parameters were employed: repetition time = 20 s, echo time = 1.4 ms, flip angle = 8°, Shinnar-Le Roux minimum-phase saturation pulse = 90° of pulse length 1 ms, FOV = 256×256 mm^2, matrix = 128×128 and 27 contiguous slices (25 slices in axial orientation) of 4 mm thickness. The reference voltage was set to 260 V for all acquired images to ensure equal input power. B_1^+ field maps in sagittal orientation were reconstructed by interpolating the axial data using MATLAB (MathWorks, Natick, MA) to an in-plane resolution of 4×2 mm^2/pixel. Experimental B_1^+ field profiles and B_1^+ field comparison maps for all orientations were computed using MATLAB. The comparison maps were calculated as the ratio between the meander dipoles and the reference.

3. Results

3.1. Numerical simulations of the meander dipoles

Table 1 shows the optimized lateral dimensions for each structure based on the RCS results. The chosen frequency (305 MHz) was higher than the proton Larmor frequency to balance the resonant frequency reduction from the FR-4 substrate and phantom loading in the experimental setup. This condition guarantees that the magnetic field generated by the shimming elements will constructively interfere with the magnetic field produced by the main coil.

The first orientation of the 3rd-order Hilbert fractal in Fig. 1.a is the same orientation used in Motovilova et al. [38]. A negative μ_r was found at the targeted resonance frequency accordingly. The far field shows that the structure radiates as a magnetic dipole. Once the structure is rotated by 90° (Fig. 1.b), μ_r becomes positive and ε_r turns negative. With this new orientation, the true Hilbert fractal radiates as an electric dipole. Fig. 1c shows the meander dipole in an orientation similar to the first case of the Hilbert fractal. The incident wave is normal to the shortest side. There is no coupling between the incident wave and the resonance of the structure due to the reduce lateral size. In order to resonate in this orientation, the structure should be larger. Finally, the orientation of the meander dipole in Fig. 1.d is the one used in experiments. The incident wave is normal to the longest side of the meander dipole. Similar to the

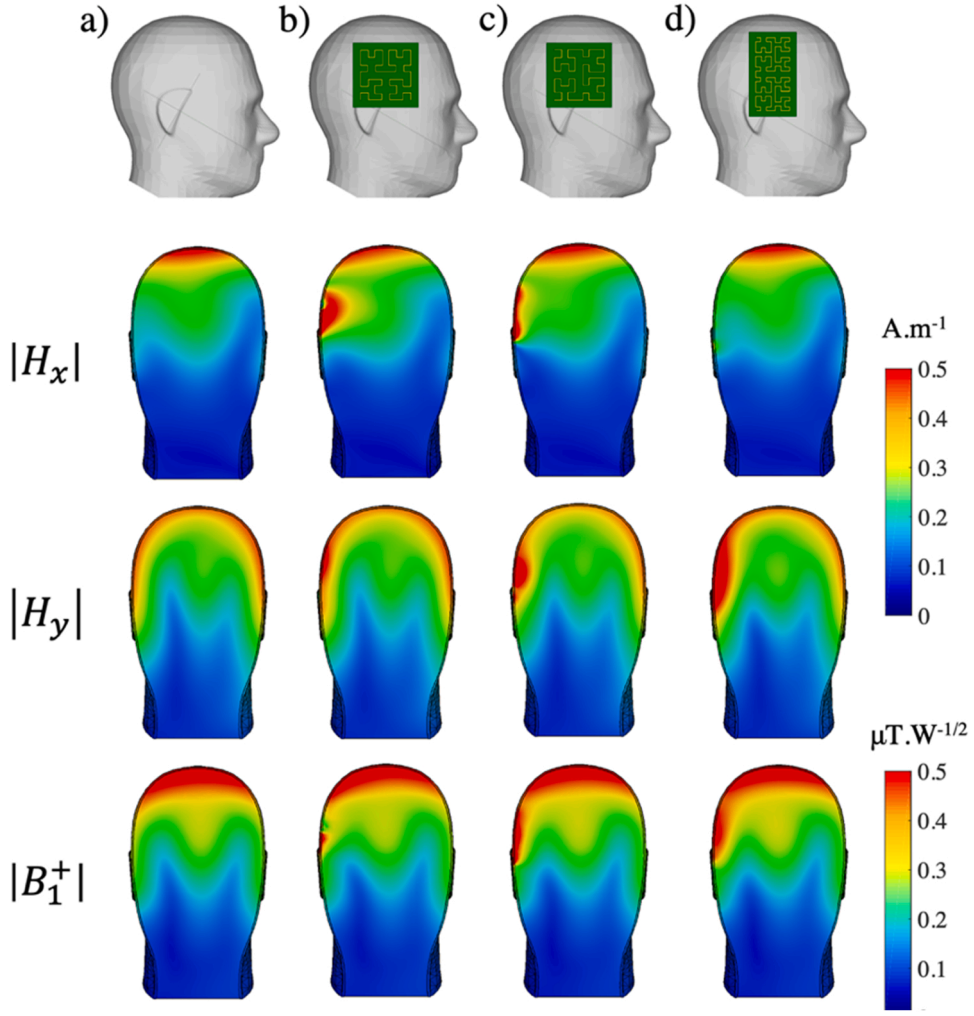

Fig. 2. Simulated magnetic (H) field and B_1^+ maps. First row, schematic of the passive structure position with respect to the phantom showing the reference (a), the true Hilbert in orientation as split-ring resonator (b), the true Hilbert with the same orientation as the meander dipole (c) and the meander dipole (d). Second and third rows, H_x and H_y maps in A/m on central coronal slices. The last row shows the corresponding B_1^+ maps in $\mu T/W^{1/2}$.

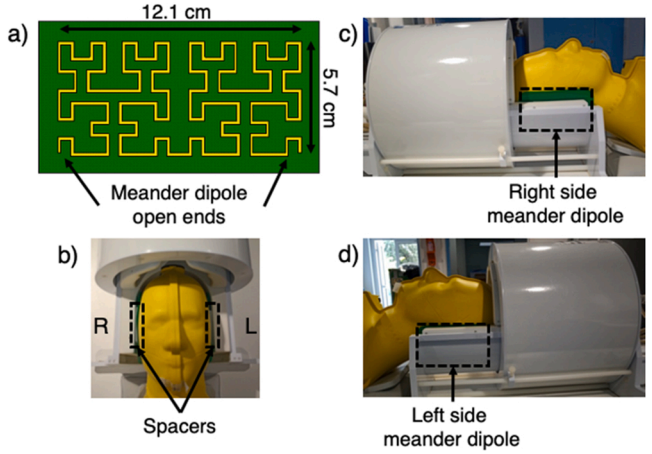

Fig. 3. Experimental setup. a) meander dipole schematic showing the open ends and b) placement of the structures inside the head coil. The meander dipoles are place on each side, close to the phantom. In order to keep this position, foam spacers were used as support. Position of the meander dipoles seen from the c) right and d) left side.

Table 1
Optimized dimensions of the true Hilbert curve and meander dipole using different fractal orders. In each case the structure resonates at 305 MHz.

Fractal order	True Hilbert dimensions in cm	Meander dipole dimensions in cm
2	11.3 × 11.3	17.2 × 7.1
3	7.5 × 7.5	12.1 × 5.7
4	5.3 × 5.3	8.2 × 3.9

case for the Hilbert fractal in Fig. 1.b, the meander dipole presents a negative ε_r. Its radiation pattern is similar to a straight electric dipole.

Fig. 2 presents the H field components maps and resulting B_1^+ maps for the meander dipole and the two orientations of the true Hilbert fractal. The reference images (Fig. 2.a, e.g. head coil alone) show the characteristic H field and B_1^+ field inhomogeneities in the temporal regions of the brain that are typically visible at UHF. The Hilbert fractal in the first case (Fig. 2.b) produces mostly H_x component. The rotated Hilbert fractal (Fig. 2.c) produces a combination of H_x and H_y components. The meander dipole produces mostly H_y component (Fig. 2.d). As expected in the B_1^+ maps, a strong effect can be spotted from the meander dipole, and slightly less from the rotated true Hilbert (same orientation as the meander dipole). In contrast, we can see that the Hilbert fractal from the first case presents less impact on the B_1^+ distribution.

The simulated B_1^+ maps obtained from the head coil alone (Ref), two passive meander dipoles inductively coupled to the head coil, and with small and large dielectric pads are shown in Fig. 4. The maps acquired with the meander dipoles show a local enhancement of the B_1^+ field. The effect is strongly visible close to the meander dipoles (green boxes) in the coronal and axial slices, outrunning the effect of the small dielectric pads at the temporal regions. However, the large pads show a significant improvement of the targeted area, with significant field loss in other regions such as the frontal and the occipital.

The simulated B_1^+ field profiles in Fig. 5 show the local field enhancement obtained in the sagittal and coronal slices, as well as in the three axial slices. Averaging over the coronal and the first two axial slices we found a 1.7-fold higher field at the local minimum of the reference (e.g. positions − 6 cm and 6 cm), whereas in the third axial slice the enhancement at these positions was 1.3-fold. In the sagittal slice, the profile is slightly shifted towards the posterior side of the head. The average deviation between meander dipole and reference profiles is 5% ± 3%.

Fig. 6 shows the B_1^+ field distribution maps and Fig. 7 shows their respective profiles obtained from the body voxel model Hugo. The effect was localized on the temporal sides of the brain and comparable to that obtained with the homogeneous phantom. At positions − 6 cm and 6 cm (local minimum of the reference) on the coronal/axial profile in Fig. 7, the B_1^+ gain was 1.76 and 1.32, respectively.

Table 2 shows the global and local SAR calculations from Hugo. A slight increase in both global SAR (1.4%) and local SAR (0.7%) can be seen. Furthermore, the location of the maximum SAR was at the same relative position, from which it can be deduced that the meander dipoles do not drastically change the electric field distribution.

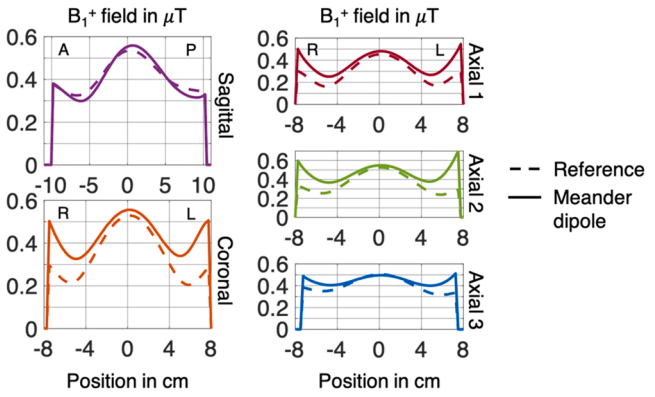

Fig. 5. Numerically B_1^+ profiles of the head coil alone (dashed lines) and with the meander dipoles (in solid lines) for each of the chosen slices.

3.2. Phantom experiments with two meander dipoles

The experimental B_1^+ maps in Fig. 8 show the effect of the meander dipoles in a central sagittal slice, a coronal slice and three axial slices. The presence of the meander dipoles leads to a significant local B_1^+ enhancement. In the last row, comparison maps are shown to quantitatively evaluate the relative B_1^+ increase. They clearly show the enhanced locations. The temporal lobe ROIs from the axial reference scan (e.g. first row) are represented by the dashed shapes. The mean gain values obtained inside each ROI are shown at the bottom of the figure. In the sagittal comparison map a 2% average loss of the field was calculated.

The experimental B_1^+ field profiles in Fig. 9 show the field enhancement obtained in the sagittal slice, the coronal slice and in the

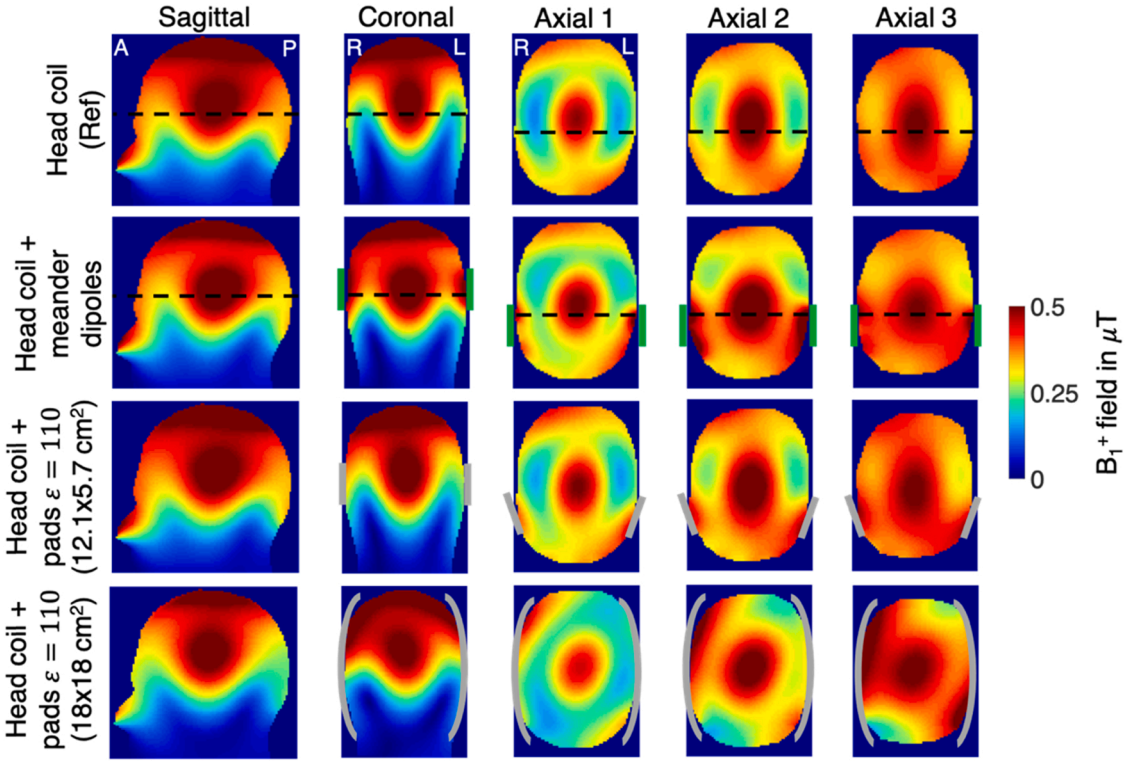

Fig. 4. Simulated B_1^+ maps of the head coil alone (reference, first row), with the meander dipoles (second row) and with small and large dielectric pads with a $\varepsilon_r = 110$ (third and fourth rows respectively). The dashed lines represent the location where the profiles shown in Fig. 5 were extracted. Additionally, the dashed line on the sagittal slice shows the location of the lower axial slice, axial 1, and the dashed lines on the axial slices show the location of the coronal slice. The sagittal slice was taken from the center of the phantom. The green rectangles on the second raw represent the relative position of the meander dipoles in the simulation. The gray rectangles represent the relative position of the dielectric pads. The letters A, P, R and L designate the anterior, posterior, right and left sides of the phantom.

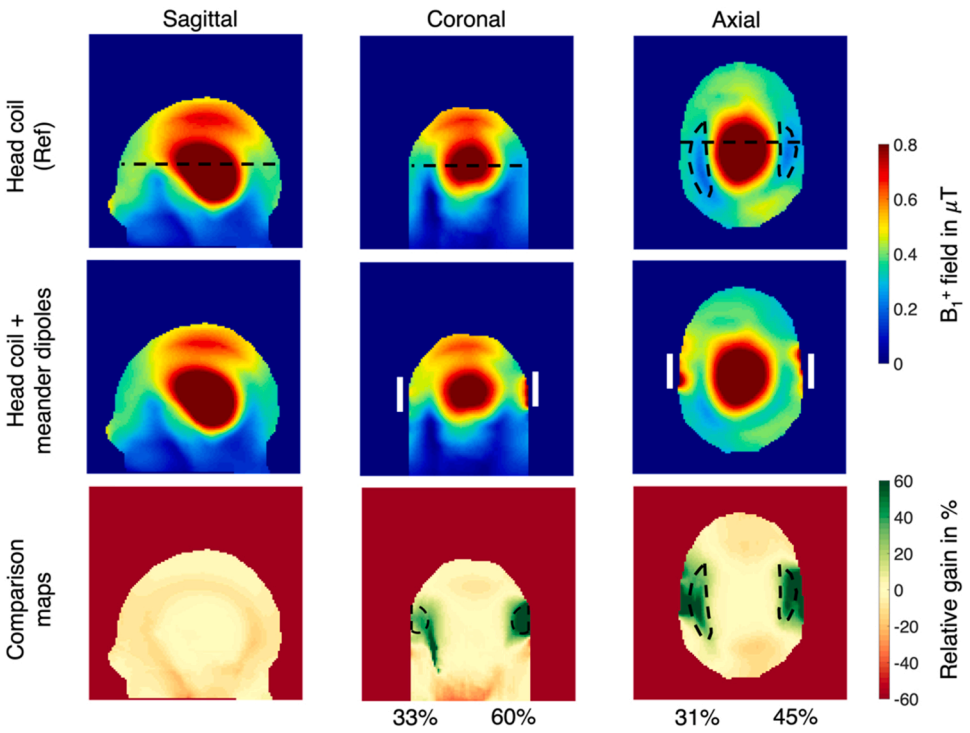

Fig. 6. Simulated B_1^+ maps on Hugo from the voxel family shown in the three main orientations with the head coil alone (reference, first row) and in presence of the meander dipoles (second row). The bottom row shows the comparison maps between the meander dipoles and the reference in percent. The dashed lines represent the location of the profiles shown in Fig. 7 as well as the location of the other slices where the profiles were extracted. The dashed areas delimit the ROIs in which the average gain was calculated.

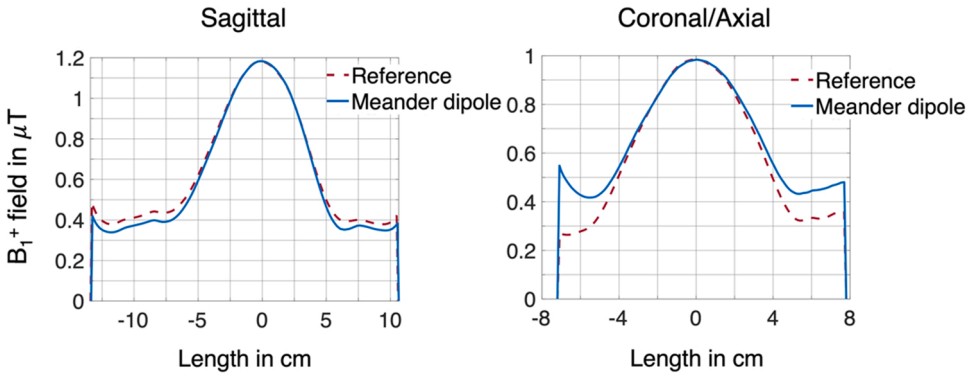

Fig. 7. Simulated B_1^+ profiles on Hugo from the voxel family with the head coil alone (reference in dashed lines) and with the meander dipoles (in solid lines). For coronal and axial slices, the profile was obtained from the same location.

Table 2
Global and local SAR results on Hugo from the voxel family.

	Hugo simulation	
	Reference	Meander dipole
Global SAR W/Kg	0.147	0.149 (+ 1.4%)
Local SAR (10 g) W/Kg	0.568	0.572 (+ 0.7%)

three axial slices. The strongest effect can be seen in the coronal and in the first two axial slices. At the local minimum over these slices (e.g. positions − 6 cm and 6 cm), the average field increment while using the meander dipoles was 1.6-fold. The profile in the highest axial slice shows a 1.2-fold enhancement. In the sagittal slice, the reference curve and the meander dipole curve have the same behavior (average deviation 1.5% ± 1.5%).

4. Discussion

We proposed and evaluated a specifically designed meander dipole using numerical simulations as well as phantom experiments in a 7 T MRI system. We based our design on Hilbert fractals since they are well known for their space-filling properties. Space-filling property, also known as fractal dimension, is the ability of a fractal to meander in such way that all the space is filled [36,37]. Hilbert fractal-based antennas, in the form of monopoles, loops and dipoles, usually have an electrically small size (e.g. length $\leq \lambda/10$) and improved radiation characteristics [44–46]. While fractals are well known in telecommunication applications, only few applications have been explored in MRI. One example is the Koch loop, based on the Koch fractal, which was used as a solution for eliminating mutual inductance [47] as well as for a new coil for ^{129}Xe lung imaging [48], both studied at 3 T. Another reported example is a surface coil consisting of a non-modified 4th-order Hilbert fractal copper structure coupled with a microstrip line [38]. A recent study reported on a multi-loop RF coil to improve coil sensitivity. The coil consisted of a single element formed by a group of small loops connected in series [49]. Although this study was not based on a proper fractal design, it considers a similar space-filling property for the design of the structure.

The tuning of the meander dipole without using lumped elements

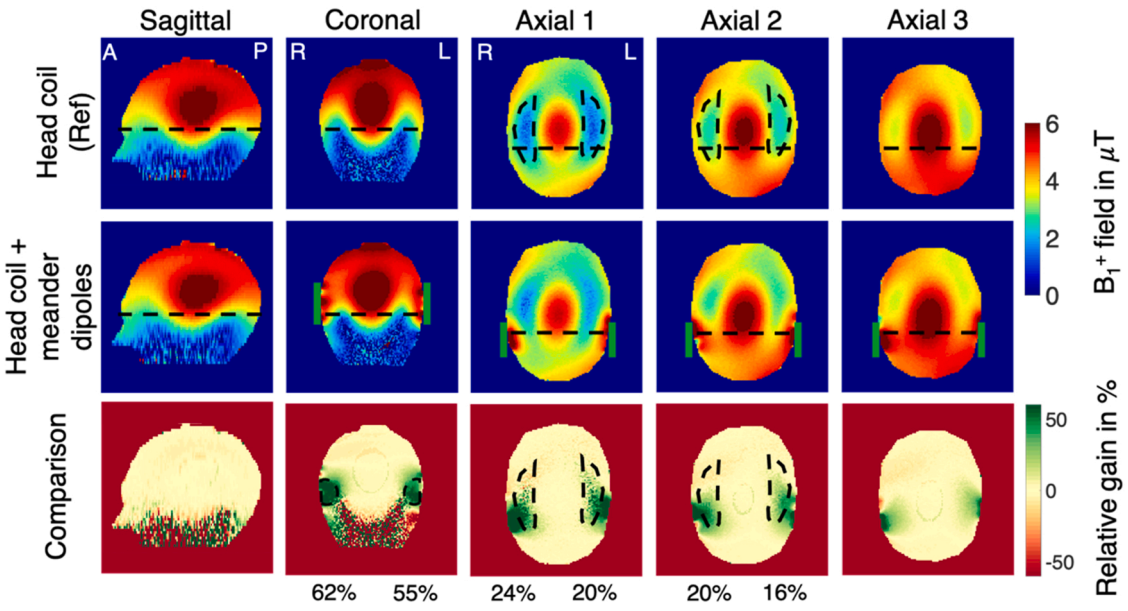

Fig. 8. Experimental B_1^+ field maps obtained on a phantom. A central sagittal slice, a coronal slice, and three different axial slices show the B_1^+ field distribution of the head coil alone (reference, first row) and with the resonant meander dipoles added (second row). The dashed lines represent the location of the profiles shown in Fig. 9 and the location of the other slices. The dashed shape delimits the ROIs in which the average gain was calculated. The bottom row shows the difference maps in percentage between the meander dipoles and the reference. The letters A, P, R and L designate the anterior, posterior, right and left sides of the phantom.

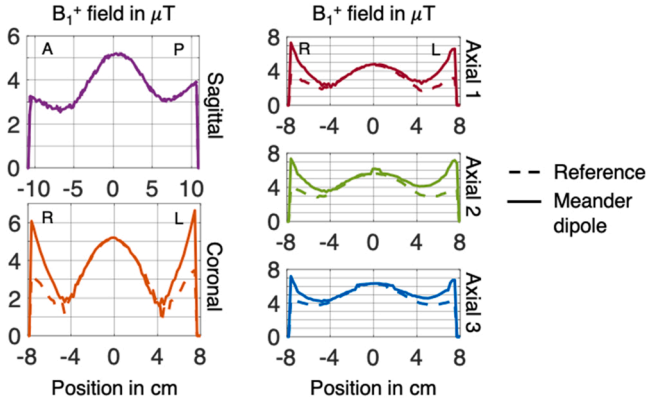

Fig. 9. Experimental B_1^+ profiles of the head coil alone (reference in dashed lines) and with the meander dipoles (in solid lines) for each of the slices shown in the field maps.

can be done by adapting its size and adjusting the gap between the meander dipole and the phantom. The use of lumped elements would indeed be disadvantageous since tuning the lumped elements at high magnetic fields (high frequencies) becomes difficult due to the increasing stray capacitance [15]. We decided to use the size adaptation as tunning method based on the RCS results. Table 1 shows the optimized dimensions of three different fractal orders of the true Hilbert fractal and the meander dipole. Our goal was to obtain an electric dipole like resonator that could fit within the dimensions of state-of-the-art dielectric pads while significantly reducing the thickness. Different permittivity and dimensions of dielectric pads targeting the brain temporal lobes at 7 T have been studied. One of the first dielectric pads proposed were made of distilled water ($\varepsilon_r = 78$, $\sigma = 0.87$ S/m) with a dimension of $16 \times 6 \times 4$ cm^3 [4]. Higher permittivities were required to reduce the pad thickness, leading to the introduction of perovskite aqueous materials. $CaTiO_3$ pads of $\varepsilon_r = 110$ and $\sigma = 0.05$ S/m with $18 \times 18 \times 2$ cm^3 dimensions were first introduce due to its availability and relative low cost [50]. It was later shown that the efficiency of the $CaTiO_3$ pads was not degraded when reducing the thickness to 1 cm [51]. $CaTiO_3$ pads with 0.8 cm thickness were employed using $\varepsilon_r = 110$ with $\sigma = 0.05$ S/m [24] and $\varepsilon_r = 150$ with $\sigma = 0.13$ S/m [52]. Meanwhile, $BaTiO_3$ mixtures were explored since higher permittivities (between 150 and 350) could be achieved and thus thinner pads [5,6]. Numerical studies on $BaTiO_3$ pads showed that the optimal permittivity for $18 \times 18 \times 0.5$ cm^3 pads was $\varepsilon_r = 150$ and $\sigma = 0.04$ S/m [26]. It has been shown that smaller $BaTiO_3$ pads could be designed, $10 \times 10 \times 0.5$ cm^3, with $\varepsilon_r = 350$ and $\sigma = 0.96$ S/m [6]. We decided to choose the lateral dimensions of our shimming elements based on the most compact design explored in dielectric pads. Consequently, the 3rd-order Hilbert fractal-based meander dipole was the closest to the targeted dimensions.

We numerically studied the EM behavior of the two possible orientations of the true Hilbert fractal and the meander dipole (Fig. 1) as well as their produced H field components and the resulting B_1^+ distribution (Fig. 2). In order to obtain a negative relative permeability μ_r, similar to a split-ring resonator [53], the Hilbert fractal requires a specific orientation with respect to the incoming field. The virtual line connecting the open ends of the structure should be perpendicular to the incoming E field and the H field should be normal to the plane containing the structure, as shown in Fig. 1.a. It has been shown that this particular orientation of the true Hilbert fractal is effective enhancing the sensitivity of surface coils, such as microstrips [38]. However, we have demonstrated that it is not optimal to couple with volume coils like the birdcage since it produces mainly H_x component (Fig. 2.b). The reference B_1^+ map (Fig. 2.a) suggests that the inhomogeneities captured in the H_y component dominates the resulting B_1^+ distribution in the temporal lobe region. This observation explains why the meander dipole structure (producing mostly H_y magnetic field) can restore B_1^+ amplitude more efficiently in the targeted area. Furthermore, we corroborated an electric dipole-like behavior of the meander dipole by extracting the far field scattered power. We have shown that the meander dipole only responds if the virtual line connecting the open ends is aligned with the incoming electric field whereas the Hilbert fractal can couple with both orientations.

The flexibility of the structure is a consequence of the small substrate thickness. Moreover, the positioning of the structure at the level of the ears and the relatively compact size of the structure did not require

important bending when set in the coil as shown in Fig. 3.b and 3.c. The excellent agreement between numerical (no bending) and experimental results confirms that the eventual bending in our experimental setting only marginally affects the performance of the structure.

In Fig. 4, we show that the meander dipole has a stronger enhancement of B_1^+ amplitude compared to the small dielectric pads. We believe that the main effect can be attributed to the size of the pads. According to literature, the optimal size for a pad with relative permittivity of 110 and a thickness $\approx$ 1 cm should be 18×18 cm^2 [24,51]. The effect of the large dielectric pad with such size is indeed greater than the meander dipoles as shown in the last row of Fig. 4. However, it strongly disturbs the B_1^+ amplitude in other areas such as the frontal and occipital as reported in previous studies using dielectric pads [25,26].

A qualitative correspondence can be observed in the different slices and orientations shown in Figs. 4 and 8. They show a strong enhancement of the B_1^+ field when adding the passive meander dipoles. However, the enhancement was very localized, only being beneficial in the temporal lobe regions. The commonly used figures of merit for the B_1^+ field homogeneity such as NRMSE would therefore not be able to accurately reflect such a local effect.

The secondary field created by the meander dipoles is asymmetrical due to the current distribution. Similarly, to a straight dipole, the current is mainly concentrated in the center of the structure than at the ends. Therefore, the profiles extracted from Figs. 4 and 8 are located on the side of the meander dipoles (green box). We obtained a consistent 1.6-fold average enhancement of the B_1^+ field at a position where usually the temporal lobes would be located. This value is very close to the predicted 1.7-fold enhancement in the numerical simulations. It is further important to keep in mind that the experiments were carried out with a 1Tx/32Rx coil. The receive array part of the coil was not modeled in the simulation environment, which could explain the small discrepancies observed.

The simulations done with the body voxel model Hugo (Figs. 6 and 7) have demonstrated a good agreement of the effect of the meander dipoles compared to the results obtained with the homogeneous phantom. Furthermore, the body voxel family allowed a calculation of global and local SAR. The results (Table 2) show a 1.4% increase in global SAR and a 0.7% increase in local SAR. Such levels of increase would not affect the safety concerns as local SAR should remain under regulation threshold.

Other than the temporal lobes, there is a great interest in maintaining high sensitivity in other areas of the brain such as the frontal lobe and the cerebellum for applications such as functional MRI (fMRI) [54,55]. It has been demonstrated that dielectric pads locally enhance the transmit efficiency up to 3-fold in the temporal regions [26]. However, this gain was balanced with losses in the cerebellum region. In another study, the cerebellum was directly targeted, obtaining a 50% increase in that region, but associated with a 20% loss on the frontal lobe [25]. Again, the simulation results presented in Fig. 4 with large pads confirm these observations. The HMA was shown to provide a 28% average gain over the entire right hemisphere but resulted in a 34% loss in the region of the cerebellum [31]. These losses were a consequence of the strong mutual interaction between the shimming devices (e.g. dielectric pads or HMA) and the RF coil. The meander dipoles proposed in this study appear to have a lower impact on the transmit efficiency than the previous studies. However, we showed that the loss in other regions of the brain outside the targeted temporal lobes is minimal. First, this was directly confirmed by the 2% losses calculated in the sagittal difference maps in Fig. 8 and the 1.5% relative deviation obtained in the experimental sagittal profiles of Fig. 9, which was lower than the 5% predicted by the simulations. Second, it was indirectly confirmed by the fact that we did not need to modify the input power from the scanner throughout the experimental measurements. We believe that the small size of the meander dipoles was able to reduce the interelement coupling between the two passive elements across the phantom, usually observed with straight dipoles or high dielectric constant pads. Additional analyses may determine structures that can further optimize these aspects and, in particular, enable adding more than two shimming elements in the head coil.

5. Conclusion

We designed and built meander dipoles inspired from Hilbert fractals for use as passive RF shimming devices in a 7 T head coil. We showed a strong agreement between simulated and experimental results. The meander dipoles were designed to efficiently couple with the head coil, allowing significant enhancement of the B_1^+ field in the two temporal lobes while maintaining a high transmit efficiency in other ROIs. Due to their sub-millimetric thickness, the meander dipoles were easy to handle and to place between the phantom and the receive array of the head coil, which is a major advantage to maintain patient comfort. Further studies will be needed to demonstrate these benefits on healthy volunteers. Such fractal-inspired structures open possibilities in targeting other regions such as the cerebellum, which usually suffers from poor excitation in 7 T head coils.

Declaration of Competing Interest

The authors declare that they have no known competing financial interests or personal relationships that could have appeared to influence the work reported in this paper.

Acknowledgements

This project has received funding from the European Union's Horizon 2020 Research and Innovation Programme under Grant agreement no. 736937 first (M-CUBE Project), and then under Grant agreement no. 952106 (M-ONE Project); and from the Excellence Initiative of Aix-Marseille University – A*MIDEX, a french "Investissements d'Avenir" programme under Multiwave chair of Medical Imaging.

References

[1] Q.X. Yang, J. Wang, X. Zhang, C.M. Collins, M.B. Smith, H. Liu, W. Chen, et al., Analysis of wave behavior in lossy dielectric samples at high field, Magn. Reson. Med.: Off. J. Int. Soc. Magn. Reson. Med. 47 (5) (2002) 982–989.
[2] B.L. Beck, K.A. Jenkins, K. Padgett, J.R. Fitzsimmons, S.J. Blackband, Observation of B1 inhomogeneities on large biological samples at 11.1 T, in: Proceedings of the 11th Annual Meeting of ISMRM, 2003, p. 716.
[3] L.L. Wald, G.C. Wiggins, A. Potthast, C.J. Wiggins, C. Triantafyllou, Design considerations and coil comparisons for 7 T brain imaging, in: Proceedings of the 13th Annual Meeting of ISMRM, 2005, p. 921.
[4] Q.X. Yang, W. Mao, J. Wang, M.B. Smith, H. Lei, X. Zhang, W. Chen, et al., Manipulation of image intensity distribution at 7.0 T: passive RF shimming and focusing with dielectric materials, J. Magn. Reson. Imaging: Off. J. Int. Soc. Magn. Reson. Med. 24 (1) (2006) 197–202.
[5] A.G. Webb, Dielectric materials in magnetic resonance, Concepts Magn. Reson. Part A 38 (4) (2011) 148–184.
[6] A.L. Neves, L. Leroi, Z. Raolison, N. Cochinaire, T. Letertre, R. Abdeddaïm, N. Malléjac, et al., Compressed perovskite aqueous mixtures near their phase transitions show very high permittivities: new prospects for high-field MRI dielectric shimming, Magn. Reson. Med. 79 (3) (2018) 1753–1765.
[7] M.V. Vaidya, M. Lazar, C.M. Deniz, G.G. Haemer, G. Chen, M. Bruno, C.M. Collins, et al., Improved detection of fMRI activation in the cerebellum at 7T with dielectric pads extending the imaging region of a commercial head coil, J. Magn. Reson. Imaging 48 (2) (2018) 431–440.
[8] M. Dubois, L. Leroi, Z. Raolison, R. Abdeddaim, T. Antonakakis, J. de Rosny, G. Tayeb, et al., Kerker effect in ultrahigh-field magnetic resonance imaging, Phys. Rev. X 8 (3) (2018), 031083.
[9] M. Dubois, L. Leroi, Z. Raolison, R. Abdeddaim, T. Antonakakis, J. de Rosny, G. Tayeb, et al., Enhancement of transmit and receive efficiencies with hybridized meta-atom in 7 T head coil, in: Proceedings of the 27th Annual Meeting of ISMRM, 2019, p. 1491.
[10] R. Schmidt, A. Slobozhanyuk, P. Belov, A. Webb, Flexible and compact hybrid metasurfaces for enhanced ultra high field in vivo magnetic resonance imaging, Sci. Rep. 7 (1) (2017) 1–7.
[11] T.S. Ibrahim, R. Lee, B.A. Baertlein, A.M. Abduljalil, H. Zhu, P.M.L. Robitaille, Effect of RF coil excitation on field inhomogeneity at ultra high fields: a field optimized TEM resonator, Magn. Reson. Imaging 19 (10) (2001) 1339–1347.
[12] T. Vaughan, L. DelaBarre, C. Snyder, J. Tian, C. Akgun, D. Shrivastava, P. Andersen, et al., 9.4 T human MRI: preliminary results, Magn. Reson. Med.: Off. J. Int. Soc. Magn. Reson. Med. 56 (6) (2006) 1274–1282.

[13] S. Wang, J. Murphy-Boesch, H. Merkle, A.P. Koretsky, J.H. Duyn, B1 homogenization in MRI by multilayer coupled coils, IEEE Trans. Med. Imaging 28 (4) (2008) 551–554.
[14] K. Lakshmanan, M. Cloos, G.C. Wiggins, R. Brown, Improving B1 excitation in head apex by combining birdcage coil with crossed dipole elements, in: Proceedings of the 21st Annual Meeting of ISMRM, 2013, p. 2754.
[15] S.M. Hong, J.H. Park, M.K. Woo, Y.B. Kim, Z.H. Cho, New design concept of monopole antenna array for UHF 7 T MRI, Magn. Reson. Med. 71 (5) (2014) 1944–1952.
[16] G. Chen, M. Cloos, D. Sodickson, G. Wiggins, A 7 T 8 channel transmit-receive dipole array for head imaging: dipole element and coil evaluation, in: Proceedings of the 22nd Annual Meeting of ISMRM, 2010, p. 621.
[17] J. Paška, M.A. Cloos, G.C. Wiggins, A rigid, stand-off hybrid dipole, and birdcage coil array for 7 T body imaging, Magn. Reson. Med. 80 (2) (2018) 822–832.
[18] J.D. Clément, R. Gruetter, Ö. Ipek, A human cerebral and cerebellar 8–channel transceive RF dipole coil array at 7 T, Magn. Reson. Med. 81 (2) (2019) 1447–1458.
[19] J. Clément, R. Gruetter, Ö. Ipek, A combined 32–channel receive-loops/8–channel transmit-dipoles coil array for whole-brain MR imaging at 7 T, Magn. Reson. Med. 82 (3) (2019) 1229–1241.
[20] D. Hernandez, K.N. Kim, Computational evaluation for improving the| B1+ field in deep brain and cerebellum using a combination of a birdcage coil and a dipole antenna array. J. Electromagn. Waves Appl. (2020) 1–14.
[21] P. Ullmann, S. Junge, M. Wick, F. Seifert, W. Ruhm, J. Hennig, Experimental analysis of parallel excitation using dedicated coil setups and simultaneous RF transmission on multiple channels, Magn. Reson. Med.: Off. J. Int. Soc. Magn. Reson. Med. 54 (4) (2005) 994–1001.
[22] K. Setsompop, L.L. Wald, V. Alagappan, B.A. Gagoski, E. Adalsteinsson, Magnitude least squares optimization for parallel radio frequency excitation design demonstrated at 7 T with eight channels, Magn. Reson. Med.: Off. J. Int. Soc. Magn. Reson. Med. 59 (4) (2008) 908–915.
[23] R. Lattanzi, D.K. Sodickson, A.K. Grant, Y. Zhu, Electrodynamic constraints on homogeneity and radiofrequency power deposition in multiple coil excitations, Magn. Reson. Med.: Off. J. Int. Soc. Magn. Reson. Med. 61 (2) (2009) 315–334.
[24] W.M. Teeuwisse, W.M. Brink, A.G. Webb, Quantitative assessment of the effects of high-permittivity pads in 7 T MRI of the brain, Magn. Reson. Med. 67 (5) (2012) 1285–1293.
[25] K.R. O'Brien, A.W. Magill, J. Delacoste, J.P. Marques, T. Kober, H.P. Fautz, G. Krueger, et al., Dielectric pads and low-adiabatic pulses: complementary techniques to optimize structural T1w whole-brain MP2RAGE scans at 7 T, J. Magn. Reson. Imaging 40 (4) (2014) 804–812.
[26] W.M. Teeuwisse, W.M. Brink, K.N. Haines, A.G. Webb, Simulations of high permittivity materials for 7 T neuroimaging and evaluation of a new barium titanate-based dielectric, Magn. Reson. Med. 67 (4) (2012) 912–918.
[27] A. Raaijmakers, O. Ipek, D. Klomp, H. Kroeze, B. van de Bank, V. Boer, N. van den Berg, et al., High-field imaging at low SAR: Tx/Rx prostate coil array using radiative elements for efficient antenna-patient power transfer, in: Proceedings of the 18th Annual Meeting of ISMRM, 2010, p. 48.
[28] A.J.E. Raaijmakers, O. Ipek, D.W. Klomp, C. Possanzini, P.R. Harvey, J. J. Lagendijk, C.A. van Den Berg, Design of a radiative surface coil array element at 7 T: the single-side adapted dipole antenna, Magn. Reson. Med. 66 (5) (2011) 1488–1497.
[29] A.J.E. Raaijmakers, P.R. Luijten, C.A. van Den Berg, Dipole antennas for ultrahigh-field body imaging: a comparison with loop coils, NMR Biomed. 29 (9) (2016) 1122–1130.
[30] G.C. Wiggins, B. Zhang, R. Lattanzi, G. Chen, D.K. Sodickson, The electric dipole array: an attempt to match the ideal current pattern for central SNR at 7 T, in: Proceedings of the 20th Annual Meeting of ISMRM, 2012, p. 541.
[31] M. Dubois, L. Leroi, Z. Raolison, R. Abdeddaim, T. Antonakakis, J. de Rosny, G. Tayeb, et al., Passive RF shimming for 7 T head coil with hybridized meta-atom: in vivo investigation, in: Proceedings of the 28th Annual Meeting of ISMRM, 2020, p. 4093.
[32] K. Lakshmanan, M. Cloos, G.C. Wiggins, R. Brown, Improving B1 excitation in head apex by combining birdcage coil with crossed dipole elements, in: Proceedings of the 21st Annual Meeting of ISMRM, 2013, p. 2754.
[33] A.J. Raaijmakers, M. Italiaander, I.J. Voogt, P.R. Luijten, J.M. Hoogduin, D. W. Klomp, C.A. van Den Berg, The fractionated dipole antenna: a new antenna for body imaging at 7 T, Magn. Reson. Med. 75 (3) (2016) 1366–1374.
[34] A. Sadeghi-Tarakameh, A. Torrado-Carvajal, R.L. Lagore, S. Moen, X. Wu, G. Adriany, Y. Eryaman, et al., Toward human head imaging at 10.5 T using an eight-channel transmit/receive array of bumped fractionated dipoles, in: Proceedings of the 27th Annual Meeting of ISMRM, 2019, p. 430.
[35] W. Lee, M. Cloos, D.K. Sodickson, G.C. Wiggins, Parallel transceiver array design using the modified folded dipole for 7 T body applications, in: Proceedings of the 21st Annual Meeting ISMRM, 2013, p. 292.
[36] W.J. Krzysztofik, Fractal geometry in electromagnetics applications-from antenna to metamaterials, Microw. Rev. 19 (2) (2013).
[37] J. Anguera, A. Andújar, J. Jayasinghe, V.V.S.S. Chakravarthy, P.S.R. Chowdary, J. L. Pijoan, C. Cattani, et al., Fractal antennas: an historical perspective, Fractal Fract. 4 (1) (2020) 3.
[38] E. Motovilova, S.Y. Huang, Hilbert curve-based metasurface to enhance sensitivity of radio frequency coils for 7-T MRI, IEEE Trans. Microw. Theory Tech. 67 (2) (2018) 615–625.
[39] A.M. Nicolson, G.F. Ross, Measurement of the intrinsic properties of materials by time-domain techniques, IEEE Trans. Instrum. Meas. 19 (4) (1970) 377–382.
[40] W.B. Weir, Automatic measurement of complex dielectric constant and permeability at microwave frequencies, Proc. IEEE 62 (1) (1974) 33–36.
[41] D.R. Smith, D.C. Vier, T. Koschny, C.M. Soukoulis, Electromagnetic parameter retrieval from inhomogeneous metamaterials, Phys. Rev. E 71 (3) (2005), 036617.
[42] R. Abdeddaim, A. Ourir, J. de Rosny, Realizing a negative index metamaterial by con-trolling hybridization of trapped modes, Phys. Rev. B 83 (3) (2011), 033101.
[43] A. Amadon, F. Mauconduit, A. Vignaud, N. Boulant, Slice profile corrections in the XFL (magnetization-prepared turbo-FLASH) B1-mapping sequence, in: Proceedings of the 23th Annual Meeting ISMRM, 2015, p. 2377.
[44] J. Anguera, C. Puente, E. Martinez, E. Rozan, The fractal Hilbert monopole: a two-dimensional wire, Microw. Opt. Technol. Lett. 36 (2) (2003) 102–104.
[45] N. Engheta, R.W. Ziolkowski (Eds.), Metamaterials: Physics and Engineering Explorations, John Wiley & Sons, 2006.
[46] V. Radonić, G. Mišković, V. Cmojević-Bengin, Fractal dipole antennas based on Hilbert curves with different line-to-spacing ratio, in: Proceedings of the 13th International Conference on Advanced Technologies, Systems and Services in Telecommunications (TELSIKS), IEEE, 2017, pp. 95–8.
[47] S. Ha, W.W. Roeck, O. Nalcioglu, U.S. Patent No. 9,784,806, U.S. Patent and Trademark Office, Washington, DC, 2017.
[48] O.M. Dona-Lemus, N.B. Konyer, M.D. Noseworthy, Micro-strip surface coils using fractal geometry for 129Xe lung imaging applications, in: Proceedings of the 26th Annual Meeting ISMRM, 2018, p. 2377.
[49] R. Frass-Kriegl, S. Hosseinnezhadian, M. Poirier-Quinot, E. Laistler, J.C. Ginefri, Multi-loop radio frequency coil elements for magnetic resonance imaging: theory, simulation and experimental investigation, FrP 7 (2019) 237.
[50] K. Haines, N.B. Smith, A.G. Webb, New high dielectric constant materials for tailoring the B1+ distribution at high magnetic fields, J. Magn. Reson. 203 (2) (2010) 323–327.
[51] J.E.M. Snaar, W.M. Teeuwisse, M.J. Versluis, M.A. van Buchem, H.E. Kan, N. B. Smith, A.G. Webb, Improvements in high-field localized MRS of the medial temporal lobe in humans using new deformable high-dielectric materials, NMR Biomed. 24 (7) (2011) 873–879.
[52] T.P.A. O'Reilly, A.G. Webb, W.M. Brink, Practical improvements in the design of high permittivity pads for dielectric shimming in neuroimaging at 7 T, J. Magn. Reson. 270 (2016) 108–114.
[53] J.B. Pendry, A.J. Holden, D.J. Robbins, W.J. Stewart, Magnetism from conductors and enhanced nonlinear phenomena, IEEE Trans. Microw. Theory Tech. 47 (11) (1999) 2075–2084.
[54] R.L. Buckner, W. Koutstaal, D.L. Schacter, B.R. Rosen, Functional MRI evidence for a role of frontal and inferior temporal cortex in amodal components of priming, Brain 123 (3) (2000) 620–640.
[55] C.J. Stoodley, E.M. Valera, J.D. Schmahmann, Functional topography of the cerebellum for motor and cognitive tasks: an fMRI study, Neuroimage 59 (2) (2012) 1560–1570.